Updated spectral radiance calibration on TIR bands for TANSO-FTS-2 onboard GOSAT-2

Hiroshi Suto[1], Fumie Kataoka[2], Robert O. Knuteson[3], Kei Shiomi[1], Nobuhiro Kikuchi[1], Akihiko Kuze[1]

[1]Japan Aerospace Exploration Agency, Tsukuba-city, Ibaraki, 305-8505, Japan
[2]Remote Sensing Technology Center of Japan, Tsukuba-city, Ibaraki, 305-8505, Japan
[3]University of Wisconsin-Madison, Madison, WI, 53706, USA

Correspondence to: Hiroshi Suto (suto.hiroshi@jaxa.jp)

Abstract. The Thermal and Near-Infrared Sensor for Carbon Observation Fourier-Transform Spectrometer-2 (TANSO-FTS-2) onboard the Japanese Greenhouse gases Observing SATellite-2 (GOSAT-2) observes a wide spectral region of the atmosphere, from the ShortWave-InfraRed (SWIR) to the longwave Thermal InfraRed radiation (TIR) with 0.2 cm^{-1} spectral sampling and the corresponded spectral resolution (Full Width at Half Maximum: FWHM) of TIR region is less than 0.27 cm^{-1}. TANSO-FTS-2 has operated nominally since Feb 2019, and the atmospheric radiance spectra it has acquired have been released to the public. This paper describes an updated model for spectral radiance calibration and its validation. The model applies to the version v210210 TIR products of TANSO-FTS-2 and integrates polarization sensitivity correction for the internal optics and the pointing mirror thermal emission. These correction parameters are characterized by an optimization which depends on the difference between the spectral radiance of TANSO-FTS-2 and coincident nadir observation data from the Infrared Atmospheric Sounding Interferometer (IASI) on METOP-B. To validate the updated spectral radiance product against other satellite products, temporally and spatially coincident observation points were considered for Simultaneous Nadir Overpass (SNO) from February 2019 to March 2021 from the Atmospheric Infrared Sounder (AIRS) on Aqua, IASI on METOP-B, and TANSO-FTS on GOSAT. The agreement of brightness temperatures between TANSO-FTS-2 and AIRS and IASI was better than 0.3 K (1σ) from 180 K to 330 K for the 680 cm^{-1} CO_2 spectral range. The brightness temperatures between TANSO-FTS-2 and TANSO-FTS of version v230231, which implemented a new polarization reflectivity of the pointing mirror and was released in June 2021, generally agree from 220 K to 320 K. However, there is a discrepancy at lower brightness temperatures, pronounced for CO_2 spectral ranges at high latitudes. To characterize the spectral radiance bias for along-track and cross-track angles, a 2-Orthogonal Simultaneous Off-Nadir Overpass (2O-SONO) is now done for TANSO-FTS-2 and IASI, TANSO-FTS-2 and AIRS, and TANSO-FTS-2 and TANSO-FTS. The 2O-SONO comparison results indicate that the TIR product for TANSO-FTS-2 has a bias that exceeds 0.5 K in the CO_2 spectral range for scenes with forward and backward viewing angles greater than 20°. These multi-satellite sensor and multi-angle comparison results suggest that the calibration of spectral radiance for TANSO-FTS-2 TIR, version v210210, is superior to that of the previous

version in its consistency of multi-satellite sensor data. In addition, the paper identifies the remaining challenging issues in current TIR products.

1 Introduction

Greenhouse gases Observing SATellite-2 (GOSAT-2), was launched on 29 October 2018, to extend the success of the Greenhouse gases Observing SATellite (GOSAT) (Kuze et al., 2009, 2012, 2016) mission. It carried the Thermal And Near infrared Sensor for carbon Observation Fourier-Transform Spectrometer-2 (TANSO-FTS-2) (Suto et al., 2021). To provide continuous monitoring of the global distribution of X_{CO2} and X_{CH4}, GOSAT-2 measures both the ShortWave InfraRed (SWIR) solar radiation reflected from the Earth's surface and the Thermal InfraRed (TIR) radiation from the ground and the atmosphere. GOSAT-2 has extended SWIR spectral coverage beyond GOSAT capabilities. One extension is toward the shortwave for solar-induced fluorescence; another is toward the longwave for carbon monoxide (CO) in the 2.3 µm region. Also, TIR spectral coverage is divided into two regions, band 4 (5.5 – 8.6 µm) and band 5 (8.6 – 14.3 µm). Simultaneous spectral radiance observation for SWIR and TIR supports retrieving new partial column concentration of CO_2 and CH_4 as well as the total column concentration which are conventional products. The partial column concentration has sensitivities for the near surface (ground to around 4 km altitude) and upper troposphere (between 4 and around 12 km altitude) of CO_2 and CH_4 concentrations. These products lead to new applications for local emission estimation (Kuze et al., 2022).

The calibrated spectral radiance is essential to provide consistent products for greenhouse-gas-observing satellites such as GOSAT, Orbiting Carbon Observatory-2 (OCO-2) in orbit since July 2014 (Crisp et al., 2004, 2008, 2017), Orbiting Carbon Observatory-3 (OCO-3) in orbit since May 2019 (Eldering et al., 2019), the Sentinel-5 Precursor/TROPOspheric Monitoring Instrument (TROPOMI) in orbit since October 2017 (S5P) (Hu et al., 2018), and also the TIR sounders such as Infrared Atmospheric Sounding Interferometer (IASI) on METOP-B (Clebaux et al., 2009) and Atmospheric Infrared Sounder (AIRS) on Aqua (Aumann et al., 2003). During GOSAT-2's first year of operation, several calibration processes for characterizing TANSO-FTS-2 were carried out with onboard calibrators, as reported in Suto et al., 2021. In the early stage of TANSO-FTS-2 calibration, we found a challenging issue with the TIR products, a brightness temperature bias for lower scene temperatures.

To reduce this bias, we reassessed the calibration model for the TIR bands of TANSO-FTS-2. The new calibration model and optimized calibration coefficients were derived by comparing well-characterized sensor data from other satellites. To provide the radiometric and spectral consistency among the TIR sounders as well as the accurate partial column concentration, the angle dependent or scene radiance dependent bias in radiance spectral domain is undesirable. Then, we showed that the spectral radiance for TANSO-FTS-2 TIR bands is consistent with the intercalibration data of the other TIR sounders mentioned above, with time-series, wavenumber, and the incident angle dependencies.

This paper first introduces an updated instrument calibration model for TANSO-FTS-2 TIR bands. A description of the optimization procedure follows for calibration coefficients, such as non-linear response, polarization sensitivity, pointing mirror reflection, and pointing mirror's thermal emission. Next is a validation of updated radiance data with the first two years of in-orbit performance compared to temporally and spatially coincident data for Simultaneous Nadir Overpasses (SNOs) from other satellites. Furthermore, these data were acquired for cross-track, along-track 2-Orthogonal Simultaneous Off-Nadir Overpass (2O-SONO) data from other TIR sounders to validate multi-angle consistency.

2 Instrument calibration models

All the processing from interferogram to atmospheric radiance spectra for TANSO-FTS-2 was performed on the ground. The basic procedure is described in the GOSAT-2 Level-1 Algorithm Theoretical Basis Document (GOSAT-2 FTS-2 L1 ATBD, 2020) and Suto et al., 2021. As described in the previous paper, version v102102 of the TIR product has applied an empirical bias correction coefficient to reduce the brightness temperature bias for TANSO-FTS-2 product. However, that product still has a low brightness temperature bias for cold scenes against the other coincident satellite data comparisons. To update the physical model for correcting the low brightness temperature bias, the non-linear response of the infrared detectors, polarization sensitivity of internal optics, and thermal emission from pointing mirror are reassessed in this paper.

2.1 Non-linear correction

In level 1 processing, the raw digital signals are converted into physical units. For TANSO-FTS-2, an interferogram was constructed with a DC offset and gain correction. The simplified equation for conversion from raw digital units to physical units is described by equation (1).

$$I\_amp_b = \frac{ADC\_scale_b}{PGA\_gain_b} DN_b + DAC\_scale_b DC\_offset_b + V\_offset_b \tag{1}$$

where

b: Bands (bands 4, 5)

I_amp_b: Interferogram with DC offset and gain correction applied.

ADC_scale_b: Analog-to-digital conversion scale

DN_b : Digital count for each interferogram

PGA_gain_b: Gain factor for each band

DAC_scale_b: Digital-to-analog conversion factor for each band

DC_offset_b : DC offset clamped at start of observation

V_offset_b: Offset signal

If the detector electronic chains have a non-linear response, the non-linear correction is applied in the interferogram domain as conventional signal processing. Equation (2) expresses the non-linear signal correction with quadratic and cubic terms. Here, a_nlc_b, b_nlc_b and c_nlc_b are non-linear coefficients for the quadratic factor, cubic factor, and offset, respectively.

$$I\_nlc_b = I\_amp_b - a\_nlc_b I\_amp_b^2 - b\_nlc_b I\_amp_b^3 + c\_nlc_b \tag{2}$$

A Photo Conductive – Mercury Cadmium Telluride (PC-MCT) detector has a non-linear response with a quadratic term. The following model considers only the linear and quadratic terms (neglecting the cubic one).

Nominally, interferogram signals have both AC and DC components. Then, the interferogram signals for each band (b) can be described with AC_b and DC_b components, as shown by equation (3).

$$I\_amp_b = AC_b + DC_b \tag{3}$$

In this case, equation (2) with a quadratic term only is rewritten as equation (4)

$$I\_nlc_b = -a\_nlc_b AC_b^2 + (1 - 2a\_nlc_b DC_b)AC_b + (DC_b - a\_nlc_b DC_b^2) \tag{4}$$

During the fast-Fourier transform numerical processing, the term of $(DC_b - a\_nlc_b DC_b^2)$ are suppressed. As a result of the fast-Fourier transform, equation (4) is converted to equation (5)

$$fft(I\_nlc_b) = -a\_nlc_b(S_b \otimes S_b) + (1 - 2a\_nlc_b DC_b)S_b \tag{5}$$

where

$S_b = fft(AC_b)$

fft : Fast-Fourier transform operator

$\otimes$: Convolution operator

In the spectral domain, the S_b component contains the in-band signal whereas the $S_b \otimes S_b$ component is the second harmonic which is mainly outside the in-band region but in principle could overlap the edges of the in-band signal. Figure 1 shows the S_b and $S_b \otimes S_b$ signals in the spectral domain for both TANSO-FTS and TANSO-FTS-2. Both TANSO-FTS and TANSO-FTS-2 have a wideband TIR channel; however, the TIR channel of TANSO-FTS-2 is separated into two bands regions. As shown in Fig. 1, $S_b \otimes S_b$ components (blue lines in Fig. 1.) overlap in the in-band signal (black lines) region for TANSO-FTS band 4, and it is prohibitively difficult to remove these components. In contrast, the $S_b \otimes S_b$ component is fully separated in TANSO-FTS-2 bands 4 and 5, and these components are negligible in the spectral domain. The signal in the spectral domain is expressed as equation (6).

$$fft(I\_nlc_b) \sim (1 - 2a\_nlc_b DC_b) S_b \tag{6}$$

This equation suggests that a non-linear correction can be applied in the spectral domain with only the non-linear coefficient a_nlc_b , the DC_b component, and the in-band spectrum S_b.

2.2 Polarization correction model

In a previous paper (Suto et al., 2021), we reported the low brightness temperature bias in TIR bands 4 and 5 for the version v102102 product. To correct this bias, we implemented a polarization sensitivity correction for TANSO-FTS-2 because the internal optical components are based on the high-polarization-sensitivity materials, such as ZnSe. To account for the polarization sensitivity correction for the version v210210 level 1 algorithm, the calibration equations are modified from those of version v102102.

The detailed polarization sensitivity of TANSO-FTS-2 optics is modeled by Stokes vectors and Müller matrices, as expressed in the optical efficiency of the FTS mechanism and aft-optics, phase difference due to the pointing mirror reflectivity, and CT rotation angle (called θ_{CT} in the following), respectively (M_{opt}, M_r, M_ε and M_{mirror} are Müller matrices of two orthogonal polarization beam splitters). S_{T_output} is output signal for Stokes vector. S_{T_input} , S_{T_mirror} , $S_{Backgroud}$ are expressed as the thermal radiation signals from observation scene, the pointing mirror and background, respectively. In this case, the S_{T_output} is expressed as equation (7).

$$S_{T\_output} = M_{opt} M_r(-\theta_{CT}) M_{mirror} M_r(\theta_{CT}) S_{T\_input} + M_{opt} M_r(-\theta_{CT}) M_\varepsilon M_r(\theta_{CT}) S_{T\_mirror} + S_{Backgroud} \tag{7}$$

where

p_1^2, q_1^2 : Pointing mirror reflectance for p- and s- polarizations (wavenumber dependence)

p_2^2, q_2^2 : Transmittance for p- and s-polarization signals for internal optics (wavenumber dependence)

L_b^{obs}: Radiance for scene temperature T^{scene} (wavenumber dependence)

$L_b^{m\_obs}$: Radiance for pointing mirror temperature T^{mirror} (wavenumber dependence)

L_b^{bb}: Radiance when viewing the calibration black body (bb) at temperature T^{bb} (wavenumber dependence)

E : The identity matrix

S_b^{obs}: The atmospheric signal (wavenumber dependence)

S_b^{bb}: The signal when viewing the calibration black body at temperature T^{bb} (wavenumber dependence)

S_b^{ds}: The deep space (ds) signal (wavenumber dependence)

$$S_{T\_input} = \begin{bmatrix} L_b^{obs} \\ 0 \\ 0 \\ 0 \end{bmatrix}$$

$$M_{opt} = \frac{1}{2}\begin{bmatrix} p_2^2 + q_2^2 & p_2^2 - q_2^2 & 0 & 0 \\ p_2^2 - q_2^2 & p_2^2 + q_2^2 & 0 & 0 \\ 0 & 0 & 2p_2q_2 & 0 \\ 0 & 0 & 0 & 2p_2q_2 \end{bmatrix}$$

$$M_{mirror} = \frac{1}{2}\begin{bmatrix} p_1^2 + q_1^2 & p_1^2 - q_1^2 & 0 & 0 \\ p_1^2 - q_1^2 & p_1^2 + q_1^2 & 0 & 0 \\ 0 & 0 & 2p_1q_1 & 0 \\ 0 & 0 & 0 & 2p_1q_1 \end{bmatrix}$$

$$M_r(\theta_{CT}) = \begin{bmatrix} 1 & 0 & 0 & 0 \\ 0 & cos2\theta_{CT} & -sin2\theta_{CT} & 0 \\ 0 & sin2\theta_{CT} & cos2\theta_{CT} & 0 \\ 0 & 0 & 0 & 1 \end{bmatrix}$$

$$M_\varepsilon = E - M_{mirror} = E - \frac{1}{2}\begin{bmatrix} p_1^2 + q_1^2 & p_1^2 - q_1^2 & 0 & 0 \\ p_1^2 - q_1^2 & p_1^2 + q_1^2 & 0 & 0 \\ 0 & 0 & 2p_1q_1 & 0 \\ 0 & 0 & 0 & 2p_1q_1 \end{bmatrix}$$

Then,

$$S_b^{obs} - S_b^{ds} = \frac{L_b^{obs}}{4}\left(\left(p_2^2 + q_2^2\right)\left(p_1^2 + q_1^2\right) + \left(p_2^2 - q_2^2\right)\left(p_1^2 - q_1^2\right)\right) - \frac{L_b^{m\_obs}}{2}\left(p_2^2 - q_2^2\right)\left(p_1^2 - q_1^2\right) \quad (8)$$

$$S_b^{bb} - S_b^{ds} = \frac{L_b^{bb}}{4}\left(\left(p_2^2 + q_2^2\right)\left(p_1^2 + q_1^2\right) - \left(p_2^2 - q_2^2\right)\left(p_1^2 - q_1^2\right)\right) \quad (9)$$

To derive the L_b^{obs} , finally, equation (10) is obtained.

$$L_b^{obs} = \left[\frac{S_b^{obs} - S_b^{ds}}{S_b^{bb} - S_b^{ds}}\right] \cdot \left[\frac{\left(p_2^2 + q_2^2\right)\left(p_1^2 + q_1^2\right) - \left(p_2^2 - q_2^2\right)\left(p_1^2 - q_1^2\right)}{\left(p_2^2 + q_2^2\right)\left(p_1^2 + q_1^2\right) + \left(p_2^2 - q_2^2\right)\left(p_1^2 - q_1^2\right)}\right] L_b^{bb} + \left[\frac{2\left(p_2^2 - q_2^2\right)\left(p_1^2 - q_1^2\right)}{\left(p_2^2 + q_2^2\right)\left(p_1^2 + q_1^2\right) + \left(p_2^2 - q_2^2\right)\left(p_1^2 - q_1^2\right)}\right] L_b^{m\_obs} \quad (10)$$

The multiplicative factor of the first term in equation (10) is called Cal_b in the following equation (11) and included the non-linearity correction.

$$Cal_b = \left[\frac{S_b^{obs} - S_b^{ds}}{S_b^{bb} - S_b^{ds}}\right] \quad (11)$$

So, if we consider the non-linear effect based on equation (6), equation (11) can be recast as equation (12).

$$Cal_b = \left[\frac{\left(1 - 2a\_nlc_b p_g DC_{obs}\right)S_b^{obs} - \left(1 - 2a\_nlc_b DC_{ds}\right)S_b^{ds}}{\left(1 - 2a\_nlc_b DC_{ict}\right)S_b^{bb} - \left(1 - 2a\_nlc_b DC_{ds}\right)S_b^{ds}}\right] = \left[\frac{\frac{\left(1 - 2a\_nlc_b p_g DC_{obs}\right)}{\left(1 - 2a\_nlc_b DC_{ds}\right)} S_b^{obs} - S_b^{ds}}{\frac{\left(1 - 2a\_nlc_b DC_{ict}\right)}{\left(1 - 2a\_nlc_b DC_{ds}\right)} S_b^{bb} - S_b^{ds}}\right] \quad (12)$$

where p_g is the Polarization sensitivity gain between different pointing mirror angles towards the black body (bb in the various symbols) or deep space (ds in the various symbols) and nadir observation. DC_b is independently observed and related to the cross-track angle. During both black body and deep space calibration, the pointing mirror is rotated along its axis by +/- 90° (from θ_{CT} =0, exact nadir observation) to view the deep space or the black body calibration target. The polarization sensitivities between calibration and nadir observation show gains due to the difference in incidence angle on the pointing mirror.

Finally,

$$L_b^{obs} = \left[\frac{\frac{(1-2a\_nlc_b p_g DC_{obs})}{(1-2a\_nlc_b DC_{ds})} S_b^{obs} - S_b^{ds}}{\frac{(1-2a\_nlc_b DC_{bb})}{(1-2a\_nlc_b DC_{ds})} S_b^{bb} - S_b^{ds}} \right] \left[\frac{(p_2^2+q_2^2)(p_1^2+q_1^2) - (p_2^2-q_2^2)(p_1^2-q_1^2)}{(p_2^2+q_2^2)(p_1^2+q_1^2) + (p_2^2-q_2^2)(p_1^2-q_1^2)} \right] L_b^{bb} + \left[\frac{2(p_2^2-q_2^2)(p_1^2-q_1^2)}{(p_2^2+q_2^2)(p_1^2+q_1^2) + (p_2^2-q_2^2)(p_1^2-q_1^2)} \right] L_b^{m\_obs} \quad (13)$$

$$DC_{obs,ds,bb} = DAC\_scale_b \cdot DC_{clamp\ for\ obs,ds,bb} + DC\_offset_b \quad (14)$$

The spectral radiance seen by TANSO-FTS-2 instrument when viewing the black body is a combination of a direct emission from the black body (at the temperature: T^{bb}) and reflected radiance originating from various external surfaces that the black body views. The view factor ($A^{bb\_baffle}, A^{PMA\_str}, A^{IOA}, A^{BS}$) for the black body bottom surface to all the external environmental surfaces that the black body can see is expressed as follows:

$$L_b^{bb} = C_b^{bb} + C_b^{bb\_baffle} + C_b^{PMA\_str} + C_b^{IOA} + C_b^{BS} \quad (15)$$

$$C_b^{bb} = \varepsilon_b^{bb} \cdot B_b^{bb}(T^{bb}) \quad (16)$$

$$C_b^{bb\_baffle} = (1-\varepsilon_b^{bb}) \cdot \varepsilon_b^{bb\_baffle} \cdot A^{bb\_baffle} \cdot B_b^{bb\_baffle}(T^{PMA+Y}) \quad (17)$$

$$C_b^{PMA\_str} = (1-\varepsilon_b^{bb}) \cdot \varepsilon_b^{PMA\_str} \cdot A^{PMA\_str} \cdot B_b^{PMA\_str}(T^{PMA-Y})$$

(18)

$$C_b^{IOA} = \left(1-\varepsilon_b^{bb}\right)\cdot\left(1-\varepsilon_b^{pointing\_mirror}\right) \cdot \varepsilon_b^{IOA}\cdot\left(A^{IOA}\right)\cdot B_b^{IOA}\left(T^{IOA+Z}\right)$$

(19)

$$C_b^{BS} = \left(1-\varepsilon_b^{bb}\right)\cdot\left(1-\varepsilon_b^{pointing\_mirror}\right) \cdot A^{BS}\cdot B_b^{BS}\left(T^{BS}\right)$$

(20)

$$A^{bb\_baffle} + A^{PMA\_str} + A^{IOA} + A^{BS} = 1$$

(21)

where

$B_b^{bb}(T^{bb})$:	Radiance for black body at a temperature T^{bb} (from housekeeping telemetry)
$B_b^{bb\_baffle}(T^{PMA+Y})$:	Radiance for black body baffle at a temperature T^{PMA+Y} (from housekeeping telemetry)
$B_b^{PMA\_str}(T^{PMA-Y})$:	Radiance for Pointing Mirror Assembly (PMA) structure panel at a temperature T^{PMA-Y} (from housekeeping telemetry)
$B_b^{IOA}(T^{IOA+Z})$:	Radiance for Integrated Optics Assembly (IOA) structure panel at a temperature T^{IOA+Z} (from housekeeping telemetry)
$B_b^{BS}(T^{BS})$:	Radiance for beam splitter (BS) at a temperature T^{BS}(from housekeeping telemetry)
$\varepsilon_b^{bb\_baffle}$:	Black body baffle surface emissivity in band b
A^{bb_baffle} :	Black body view of back body baffle
$\varepsilon_b^{PMA\_str}$:	Pointing Mechanism Assembly (PMA) structure surface emissivity in band b
A^{PMA_str}:	Black body view of PMA structure
ε_b^{IOA}:	Integrated Optics Assembly (IOA) structure surface emissivity in band b
A^{IOA} :	Black body view of IOA structure
A^{BS}:	Black body view of Beam Splitter
$\varepsilon_b^{Pointing\_mirror}$:	Pointing mirror surface emissivity in band b

2.3 Mirror reflectance model

Due to the large mirror size, it is difficult to measure the mirror reflectance onboard TANSO-FTS-2 instrument directly. During prelaunch calibration, the complex index of refraction of the mirror material (with coating) was characterized simultaneously with that of the actual flight mirror. Consequently, the pointing mirror reflectance is expressed as the following equations with the complex spectral index of refraction of the mirror coating m.

$$cos\theta_i = \frac{cos(\theta_{CT})sin(\theta_{AT}) + cos(\theta_{AT})}{\sqrt{2}} \quad (22)$$

$$r_p(m,\theta_i) = \frac{m^2 cos\theta_i - \sqrt{m^2 - sin^2\theta_i}}{m^2 cos\theta_i + \sqrt{m^2 - sin^2\theta_i}} \quad (23)$$

$$r_s(m,\theta_i) = \frac{cos\theta_i - \sqrt{m^2 - sin^2\theta_i}}{cos\theta_i + \sqrt{m^2 - sin^2\theta_i}} \quad (24)$$

$$p_1^2 = r_p(m,\theta_i) r_p^*(m,\theta_i) = \frac{\left|m^2 cos\theta_i - \sqrt{m^2 - sin^2\theta_i}\right|^2}{\left|m^2 cos\theta_i + \sqrt{m^2 - sin^2\theta_i}\right|^2} \quad (25)$$

$$q_1^2 = r_s(m,\theta_i) r_s^*(m,\theta_i) = \frac{\left|cos\theta_i - \sqrt{m^2 - sin^2\theta_i}\right|^2}{\left|cos\theta_i + \sqrt{m^2 - sin^2\theta_i}\right|^2} \quad (26)$$

A star as superscript is used for the complex conjugate in equations (25) and (26). The emissivity of the pointing mirror is expressed in equation (27).

$$\varepsilon_b^{pointing\_mirror} = 1 - \frac{1}{2}[p_1^2 + q_1^2] \quad (27)$$

3 Optimization of instrument models

The calibration equation and related models are described in the previous section. The calibration procedure must be optimized for maximum spectral radiance accuracy. In this section, the optimization procedure for the above models is discussed.

Usually, the non-linear effect of a low-temperature scene is smaller than that of high-temperature scene. We obtained the non-linear quadratic coefficient with a high-temperature target in the interferogram domain during the prelaunch calibration test. A non-linear coefficient is determined which minimizes the out-of-band signal intensity of low-frequency components.

The first term of equation (10) is the main part of the polarization effect. We assume that the difference in spectral radiance in selected spectral regions between TANSO-FTS-2 and the coincident dataset, especially at low temperatures, is directly related to polarization correction terms. We derive the ratio of p and s transmission against wavenumber based on the IASI matchup dataset. This step makes use of the value of mirror reflectance obtained during the prelaunch test where the initial parameters for polarization sensitivities are determined.

In the next step, the polarization sensitivity is further optimized with a non-linearity correction based on equation (13). In this optimization, we changed the domain from interferogram to spectra to reduce the unknown parameters with the spectra domain. As expressed in equations (1) and (2), a total of five parameters (ADC conversion scale, gain factor, DAC conversion scale, offset signal, and non-linearity correction coefficients) have to be considered to derive a precise interferogram. In contrast, in the spectral domain, the parameters are non-linear correction coefficients and DC offset as expressed in equation (12) except for polarization sensitivity gain. Then, the polarization sensitivity, non-linear correction coefficients, DC offset, and polarization sensitivity gain are optimized with equation (13) to minimize the difference of spectral radiance between TANSO-FTS-2 and IASI in SNO condition. The range of brightness temperature for the comparison between TANSO-FTS-2 and IASI is wider than that of AIRS, so the SNO condition for IASI also apply for AIRS.

The optimized results of polarization sensitivity are presented in Fig. 2. This value is applied in version v210210 products with prelaunch pointing mirror reflectance.

4 Inter-comparisons with reference satellite sensors

The comparison of TANSO-FTS-2 TIR band nadir and off-nadir comparisons provide a quantitative spectral assessment of the radiometric bias relative to the AIRS on AQUA, IASI on METOP-B, and TANSO-FTS on GOSAT.

In the following section, two types of coincident criteria are applied: SNO and cross-track, along-track 2O-SONO. Conventional weather satellites sensors, such as AIRS and IASI, have only observation capability in cross-track motion because the scanning motion is only performed in cross-track. In contrast, TANSO-FTS-2 and TANSO-FTS accommodate a two-axis agile pointing system to target the interesting observation location. Then, TANSO-FTS-2 can coordinate the cross-track of TANSO-FTS-2 and the cross-track of other satellites, and the along-track of TANSO-FTS-2 and cross-track of other satellites. The schematic diagrams of 2O-SONO coincident observation images are illustrated in Fig. 3. The coincidence criteria for SNO and 2O-SONO with satellite sensors are listed in Table 1. The coincident latitudes between AIRS and TANSO-FTS-2, between IASI and TANSO-FTS-2, and between TANSO-FTS and TANSO-FTS-2 are illustrated in both SNO (a) and 2O-SONO (b) in Fig. 4. The coincident points between the AIRS and TANSO-FTS-2 are in the mid-latitudes, and those of IASI and TANSO-FTS-2 are located at high latitudes. In contrast, the coincident points between TANSO-FTS and TASNO-FTS-2 cover the complete range of latitudes pole-to-pole. These leads to a comparison with different brightness temperature ranges for each matching dataset. We focused on the comparison in the following spectral ranges: CO_2 spectral range (681.99 - 691.66 cm^{-1}), atmospheric window channel (900.3 - 903.78 cm^{-1}), O_3 spectral range (1030.08 - 1039.69 cm^{-1}), and CH_4 spectral range (1304.36 - 1306.68 cm^{-1}) same as previous our estimation (Suto et al., 2021). Since the spectral resolution of AIRS and IASI is different from that of TANSO-FTS-2, we convolve the TANSO-FTS-2 spectra with AIRS spectral response function to comparing these data. After that, the average brightness temperature for four spectral regions is computed for both sounders. The same convolution and averaging processes are also applied to IASI data.

As for AIRS data, AIRS L1C data were applied (AIRS Science Team/Strow 2019). For the IASI, IASI-B data were selected from the NOAA CLASS archive. Aumann et al. 2019 have studied the long-term stability of AIRS spectra as compared with calculated spectra over Tropical Ocean at night and found that the trend of all AIRS longwave channels in the surface sensitive channels was quite small (2 mK/yr). In addition, AIRS and IASI are well characterized and the bias of these sensors are reported less than 0.2 K (Jouglet et al., 2014). Then, our calibration target is to provide the consistent spectral radiance among the TIR sounder for full coverage of TANSO-FTS-2 observation angles.

To compare TANSO-FTS and TANSO-FTS-2, version v230231 of TANOS-FTS, released on June 2021, was selected. This version has improved the consistency between AIRS and IASI for a better polarization coefficient of the pointing mirror.

4.1 Comparison between AIRS and TANSO-FTS-2, IASI and TANSO-FTS-2, and TANSO-FTS and TANSO-FTS-2 with SNO condition

Figure 5 shows the brightness temperature differences (TANSO-FTS-2 values minus other satellite values) in 1 K gridded bin average (mean) at four focused ranges against the atmospheric window temperature between TANSO-FTS-2 of version v210210, AIRS, IASI, and TANSO-FTS for SNO. The brightness temperature difference between TANSO-FTS-2 of version v102102 and AIRS, IASI, and TANSO-FTS are also plotted in Fig. 5 for reference. The data periods for each comparison are listed in Table 2. Figure 5 suggests that version v210210 products are more consistent with AIRS and IASI data than version v102102 in all ranges, especially in low-temperature atmospheric window. In addition, the low-temperature biases and significant deviations were removed in version v210210 products in the region around 7.6 µm covering the strong CH_4 signature. Comparing between version v210210 and version v102102, 0.5 to 1 K low-temperature biases are removed. The statistical analysis results are also summarized in Table 2. As suggested in Table 2, the standard deviation (stdv) between

TANSO-FTS-2 and AIRS, IASI is reduced with version v210210, especially in spectral ranges for CO_2 and CH_4. In comparing TANSO-FTS-2 and TANSO-FTS, the deviation is increased with version v210210. As shown in Fig. 5, in the temperature range from 180 K to 240 K, TANSO-FTS product presents large positive values against TANSO-FTS-2 for CO_2 and CH_4 spectral ranges. This means that the TANSO-FTS has inconsistent values at lower temperatures, especially for CO_2 and CH_4. In addition, the negative values are detected from 240 to 260 K in the CH_4 spectral range. The previous version of TANSO-FTS-2 has negative biases at low temperatures. The consistency between TANSO-FTS-2 and TANSO-FTS agrees in these regions. In other words, version v210210 of TANSO-FTS-2 products removes the low-temperature biases, even though TANSO-FTS version v230231 still has lower temperature biases.

Figures 6 presents the time series of the brightness temperature difference between TANSO-FTS-2 and IASI, between TANSO-FTS-2 and AIRS, and between TANSO-FTS-2 and TANSO-FTS for four spectral ranges, both versions of v210210 and v102102. During winter in the southern hemisphere, version v102102 products present negative values and large deviations due to seasonal variation, especially in the CO_2 and CH_4 spectral ranges. Cold temperature scenes over Antarctica were selected as coincident observation locations. In contrast, the version v210210 products suggest no seasonal variation except for comparison with the first TANSO-FTS instrument. These plots also indicate that version v230231 of TANSO-FTS products has a negative bias against cold scenes, observed over high-latitude coincident points.

As a result of SNO, version v210210 of TANSO-FTS-2 products show the averaged bias is less than +/-0.3 K for all four ranges. In addition, the deviations against IASI and AIRS for the CO_2 and CH_4 spectral ranges are less than 0.3 K and 0.5 K, respectively. These results suggest that the consistency for the CO_2 and CH_4 spectral ranges between TANSO-FTS-2 and AIRS, between TANSO-FTS-2 and IASI, are much improved. The comparison between TANSO-FTS-2 and TANSO-FTS shows a significant difference for low-temperature scenes but we have to conclude that version v230231 of TANSO-FTS product has a challenging issue at low temperatures, especially at high latitudes, for both CO_2 and CH_4 spectral ranges. Therefore, the calibration of the TIR band for TANSO-FTS will be updated in the next version of the level 1 product to improve the consistency of brightness temperature, especially in low-temperature high-latitude regions.

4.2 Comparison between AIRS and TANSO-FTS-2, IASI and TANSO-FTS-2, and TANSO-FTS and TANSO-FTS-2 with 2O-SONO condition

As described in the previous section, version v210210 of TANSO-FTS-2 product agrees with AIRS and IASI products in nadir coincident observations. In the next step, the comparison on 2O-SONO was made to confirm the incident angle dependency of TANSO-FTS-2 observations. The coincident conditions for 2O-SONO are listed in Table 1.

Figure 7 presents the brightness temperatures difference between TANSO-FTS-2 and AIRS, TANSO-FTS-2 and IASI, TANSO-FTS-2 and TANSO-FTS with TANSO-FTS-2 in 1° bins of the pointing mirror angles along and cross-track angles. The deviation of each bin is plotted with shaded area. The coincident observations between TANSO-FTS-2 and the AIRS in the 2O-SONO configuration presented in Figure 7 were selected with θ_{CT} (AIRS) angles in the range +40° and -40° and θ_{CT}

(TANSO-FTS-2) angles in the range +40° and -40°, whereas the related θ_{CT} (IASI) angles are in the range +20° and -20° as listed in Table 1.

Figure 7(a) shows that the brightness temperature difference between TANSO-FTS-2 and AIRS is almost stable with θ_{AT} (TANSO-FTS-2) angles in the range +/-10°. As shown in Fig. 7 (a), the brightness temperature difference between TANSO-FTS-2 and AIRS increased for larger θ_{AT} (TANSO-FTS-2) angles. In contrast, the dependence of cross-track angle plotted in Fig. 7(b) is not clear except for the CH_4 range for θ_{CT} (TANSO-FTS-2) in the range 5° to 10°.

Figures 7 (c) and (e) also present the brightness temperature difference between TANSO-FTS-2 and IASI and between TANSO-FTS-2 and TANSO-FTS against θ_{AT} (TANSO-FTS-2) angles, respectively. These plots also suggest that the brightness temperature difference depends on θ_{AT} (TANSO-FTS-2) angles. The dependence is almost flat between -10° to +10° of θ_{AT} (TANSO-FTS-2) angles. This is a similar feature to the results of the AIRS comparison. Figures 7 (d) and (f) show the brightness temperature difference between TANSO-FTS-2 and IASI and between TANSO-FTS-2 and TANSO-FTS against a θ_{CT} (TANSO-FTS-2), respectively. Figure 7 (d) suggests that the brightness temperature difference does not depend on θ_{CT} (TANSO-FTS-2) angles in the ranges of CO_2, CH_4, O_3, and in the atmospheric window region. In contrast, a cross-track dependency is observed for the CH_4 and O_3 ranges in Fig. 7 (f), which compares TANSO-FTS-2 and TANSO-FTS.

Figure 8 shows that 1° along-track (AT) by 1° cross-track (CT) grid average brightness temperature difference between TANSO-FTS-2 and the AIRS, between TANSO-FTS-2 and IASI, and between TANSO-FTS-2 and TANSO-FTS. These figures also clearly present the dependence on the along-track angle, especially in the CO_2 spectral range. For TANSO-FTS comparison, a cross-track angle dependence is also observed, even though the comparison between TANFO-FTS-2 and AIRS, between TANSO-FTS-2 and IASI are not indicated a cross-track angle dependence. Comparing Figs. 7 (f) and 8 (f), we found that the brightness temperature difference with the significant cross-track angle condition shows large biases.

As presented in Fig. 5, TANSO-FTS has a lower temperature bias in the CO_2 and CH_4 spectral ranges in a SNO. Therefore, the brightness temperature differences at four spectral ranges in the 1 K gridded average against the atmospheric window temperature are plotted in Fig. 9 for 2O-SONOs. As shown in Fig. 9, the lower temperature bias in TANSO-FTS is the same as SNO. In addition, a high-temperature bias in the CH_4 spectral range is the same as the TANSO-FTS. Therefore, we conclude that TANSO-FTS-2 does not have a cross-track dependence on TANSO-FTS. The feature is related to the brightness temperature bias in TANSO-FTS version v230231 products.

Compared with TANSO-FTS, this difference may indicate a pointing angle dependence of the pointing mirror, which is not entirely removed by the polarization correction performed in the processing v230231. The available θ_{AT} (TANSO-FTS-2) angles is +/-20°. In contrast, TANSO-FTS-2 can be set between +/-40°. In this comparison, the matchups are selected between -10° and +10° of θ_{AT} (TANSO-FTS-2) angles.

As presented in Fig. 9, the agreement between TANSO-FTS-2, AIRS, and IASI is quite satisfactory. However, the agreement between TANSO-FTS-2 and TANSO-FTS is worse than the comparison against AIRS and IASI. This suggests that the calibrated radiance of TANSO-FTS, especially in low brightness temperature regions, still has a small bias. A summary of the inter-comparisons between TANSO-FTS-2 and multi-satellite sensors with SONO is listed in Table 3.

5 Conclusions

This paper reports the performance of TANSO-FTS-2 bands 4 and 5 with the new radiance calibration method. The method is based on a non-linear response, a polarization sensitivity correction in internal optics, and pointing mirror thermal emission in the spectral domain. To evaluate its performance, the spectral radiances (level 1 processor version v210210) collected by TANSO-FTS-2 between February 2019 and October 2021 are compared to both the simultaneous nadir and 2-orthogonal off-nadir observations of the AIRS on AQUA, IASI on METOP-B, TANSO-FTS on GOSAT for the TIR bands. We conclude that the agreement between TANSO-FTS-2 and AIRS, IASI is better than 0.3 K for scenes temperatures brighter than 220 K in the CO_2 and CH_4 spectral ranges. Compared with AIRS and IASI, TANSO-FTS has a small bias on the brightness temperature for low temperatures. In the latest version of v230231 for TANSO-FTS, the polarization correction parameter for the pointing mirror is improved and officially released. For scenes with brightness temperatures around 280 K, the agreement between TANSO-FTS-2 and TANSO-FTS is quite satisfactory. However, comparisons of the 3 other infrared sensors with TANSO-FTS suggest a cold brightness temperature bias for cold scenes in high latitudes regions and this is an indication that the current products of this latter instrument have to be improved in these observation conditions. In addition, the result of 2O-SONO indicates that TANSO-FTS-2 has an along-track angle depending on bias over +/-10° along-track angle. The agreement between TANSO-FTS-2 and AIRS/IASI is good for the nominal pointing angle. However, for forward- or backward-viewing with a pointing angle greater than 20° the estimated bias exceeds 0.5 K in the CO_2 spectral range for TANSO-FTS-2 version v210210.

Data availability.

All datasets used here are publicly available and can be accessed through the links and references provided.

Author contributions.

HS wrote the manuscript and analysed data with support from FK, RO, and KS. RO, FK, KS, NK, and AK contributed to interpreting the results. FK, RO, and KS supported to the satellite inter-comparison data preparation or expertise on data sets. All authors discussed the results and contributed to the manuscript.

Competing interests.

The authors declare that they have no conflict of interest.

Acknowledgments.

The authors would like to thank Y. Yata and H. Ochi of the Mitsubishi Space Software Corporation and the members of the Japanese Ministry of the Environment, the National Institute for Environmental Studies, L3 Harris, and ABB Inc. for their cooperation.

Financial support.

This work was funded by JAXA.

References

Aumann, H. H., Chahine, M. T., Gautier, C., Goldberg, M. D., Kalnay, E., McMillin, L. M., Revercomb, H., Rosenkranz, P. W., Smith, W. L., Staelin, D. H., Strow, L. L., and Susskind, J.: AIRS/AMSU/HSB on the Aqua Mission: Design, Science Objectives, Data Products, and Processing Systems, IEEE T. Geosci. Remote, 41, 253-264, doi:10.1109/TGRS.2002.808356, 2003.

Aumann, H. H., Broberg, S., Manning, E., and Pagano, T.; Radiometric Stability Validation of 17 Years of AIRS Data Using Sea Surface Temperatures, Geophysical Research Letters, 46, 12,504–12,510. https://doi.org/10.1029/2019GL085098, 2019.

Clerbaux, C., Boynard, A., Clarisse, L., George, M., Hadji-Lazaro, J., Herbin, H., Hurtmans, D., Pommier, M., Razavi, A., Turquety, S., Wespes, C., and Coheur, P. -F.: Monitoring of atmospheric composition using thermal infrared IASI/MetOp sounder, Atmos. Chem. Phys., 9, 6041–6054, https://doi.org/10.5194/acp-9-6041-2009, 2009.

Crisp, D., Atlas, R. M., Breon, F.-M., Brown, L. R., Burrows, J.P., Ciais, P., Connor, B. J., Doney, S. C., Fung, I. Y., Jacob, D. J., Miller, C. E., O'Brien, D., Pawson, S., Randerson, J. T., Rayner, P., Salawitch, R. J., Sander, S. P., Sen, B., Stephens, G. L., Tans, P. P., Toon G. C., Wennberg, P. O., Wofsy, S. C., Yung, Y. L., Kuang, Z. M., Chudasama, B., Sprague, G., Weiss, B., Pollock, R., Kenyon, D., and Schroll, S.: The Orbiting Carbon Observatory (OCO) Mission, Adv. Space. Res., 34, 700-709, https://doi.org/10.1016/j.asr.2003.08.062, 2004.

Crisp, D., Miller, C. E., and DeCola, P. L.: NASA Orbiting Carbon Observatory: measuring the column averaged carbon dioxide mole fraction from space, J. Appl. Remote Sens., 2, 023508, https://doi.org/10.1117/1.2898457, 2008.

Crisp D, Pollock HR, Rosenberg R, Chapsky L, Lee RA, Oyafuso FA, Frankenberg C, O'Dell CW, Bruegge CJ, Doran GB, Eldering A.: The on-orbit performance of the Orbiting Carbon Observatory-2 (OCO-2) instrument and its radiometrically calibrated products, Atmos. Meas. Tech.,10, 59-81, https://doi.org/10.5194/amt-10-59-2017, 2017.

Eldering, A., Taylor, T. E., O'Dell, C.W., Pavlick, R.: The OCO-3 mission: measurement objectives and expected performance based on 1 year of simulated data, Atmos. Meas. Tech., 12, 2341-2370, doi:10.5194/amt-12-2341-2019, 2019.

GOSAT-2, Level-1 Data Description Document for TANSO-FTS- 2, available at: https://prdct.gosat-2.nies.go.jp/ja/document.html (last access: 30 March 2022), 2020.

Hu, H., Landgraf, J., Detmers, R., Borsdorff, T., Aan de Brugh, J., Aben, I., Butz, A., and Hasekamp, O.: Toward Global Mapping of Methane with TROPOMI: First Results and Intersatel- lite Comparison to GOSAT, Geophys. Res. Lett, 45, 3682–3689, https://doi.org/10.1002/2018GL077259, 2018.

Jouglet, D., Chinaud, J., Maraldi, C., Jacquette, E., Lonjou, V., Blumstein, D., Vandermarcq, O., and Lenot, X.: Radiometric and spectral inter-comparison of IASI: IASI-A / IASI-B, IASI/AIRS, IASI/CrIS, in: CALCON 2014 meeting, 12 August 2014, Salt Lake City, USA, 2014.

Kataoka, F., Knuteson, R. O., Kuze, A., Shiomi, K., Suto, H., Yoshida, J., Kondo, S., and Saitoh, N.: Calibration, Level 1 Processing and Radiometric Validation for TANSO-FTS TIR on GOSAT, IEEE T. Geosci. Remote, 57, 3490–3500, https://doi.org/10.1109/TGRS.2018.2885162, 2019.

Kuze, A., Suto, H., Nakajima, M., and Hamazaki, T.: Thermal and near infrared sensor for carbon observation Fourier-transform spectrometer on the Greenhouse Gases Observing Satellite for greenhouse gases monitoring, Appl. Opt., 48, 6716–6733, https://doi.org/10.1364/AO.48.006716, 2009.

Kuze, A., Suto, H., Shiomi, K., Urabe, T., Nakajima, M., Yoshida, J., Kawashima, T., Yamamoto, Y., Kataoka, F., and Buijs, H.: Level 1 algorithms for TANSO on GOSAT: processing and on-orbit calibrations, Atmos. Meas. Tech., 5, 2447-2467, https://doi.org/10.5194/amt-5-2447-2012, 2012.

Kuze, A., Suto, H., Shiomi, K., Kawakami, S., Tanaka, M., Ueda, Y., Deguchi, A., Yoshida, J., Yamamoto, Y., Kataoka, F., Taylor, T. E., and Buijs, H.: Update on GOSAT TANSO-FTS performance, operations, and data products after more than 6 years in space, Atmos. Meas. Tech., 9, 2445-2461, https://doi.org/10.5194/amt-9-2445-2016, 2016.

Kuze, A., Kikuchi, N., Kataoka, F., Suto, H., Shiomi, K., Kondo, Y. Detection of methane emission from a local source using GOSAT target observations., Remote Sens. 2020, 12, 267; doi:10.3390/rs12020267, 2020.

Kuze, A., Nakamura, Y., Oda, T., Yoshida, Y., Kikuchi, N., Kataoka, F., Suto, H., Shiomi, K. Examining partial-column density retrieval of lower-tropospheric CO_2 from GOSAT target observations over global megacities., 2022.

AIRS Science Team/Larrabee Strow: AIRS/Aqua L1C Infrared (IR) resampled and corrected radiances V6.7, Greenbelt, MD, USA, Goddard Earth Sciences Data and Information Services Center (GES DISC), Accessed: July 2021, 10.5067/VWD3DRC07UEN, 2019.

Suto, H., Kataoka, F., Kikuchi, N., Knuteson, R.O., Butz, A., Haun, M., Buijs, H., Shiomi, K., Imai, H., and Kuze, A.: Thermal and near-infrared sensor for carbon observation Fourier transform spectrometer-2 (TANSO-FTS-2) on the Greenhouse gases Observing SATellite-2 (GOSAT-2) during its first year in orbit, Atmos. Meas. Tech., 14, 2013-2039, https://doi.org/10.5194/amt-14-2013-2021, 2021.

Tables:

Table 1. Temporal and spatial coincidence conditions for comparing SNO and 2O-SONO

Coincidence type	Sounders	Distance between two orbits [km]	Time difference [min]	θ_{CT} for TANSO-FTS-2 [deg.]	θ_{AT} for TANSO-FTS-2 [deg.]	Distance between obs. Location [km]	AIRS scan angle [deg.]	IASI scan angle [deg.]	TANSO-FTS pointing angle [deg.]
SNO	AIRS	<+/- 100	<+/-5	<+/-3	<+/-3	<17	-	-	-
	IASI	<+/- 100	<+/-5	<+/-3	<+/-3	<17	-	-	-
	TANSO-FTS	<+/- 100	<+/-5	<+/-3	<+/-3	<17	-	-	-
2O-SONO	AIRS	<+/- 100	<+/-30	<+/-40	<+/-35	-	<+/-40	-	-
	IASI	<+/- 100	<+/-30	<+/-40	<+/-35	-	-	<+/-20	-
	TANSO-FTS	<+/- 100	<+/-30	<+/-40	<+/-35	-	-	-	<+/-15 θ_{AT} <+/-35 θ_{CT}

Table 2. Averaged brightness temperature difference (mean) and standard deviation (stdv) between TANSO-FTS-2 and 3 other infrared sounders in the SNO configuration

Sounder	No. of SNO	Version	Period	CO_2 spectral range [K]		Atmospheric window channel [K]		O_3 spectral range [K]		CH_4 spectral range [K]	
				mean	stdv	mean	stdv	mean	stdv	mean	stdv
AIRS	573	102102*	Feb. 2019-Oct. 2020	0.01	0.21	-0.63	2.55	-0.45	1.55	-0.11	1.16
IASI	1199	102102*	Feb. 2019-Mar. 2021	-0.19	0.4	-0.16	2.78	-0.43	1.37	-0.53	1.52
TANSO-FTS	72	102102*	Feb. 2019-Aug. 2020	0.16	0.28	0.0008	0.86	-0.19	0.49	-0.28	0.57
AIRS	573	210210**	Feb. 2019-Oct. 2020	0.15	0.18	-0.17	2.59	-0.01	1.56	0.11	0.41
IASI	1199	210210**	Feb. 2019-Mar. 2021	-0.1	0.26	-0.26	2.75	-0.17	1.3	0.009	0.47
TANSO-FTS	72	210210**	Feb. 2019-Aug. 2020	0.3	0.35	-0.06	0.85	0.07	0.53	-0.13	0.74

*: previous version

**: new version

Table 3. Averaged brightness temperature difference (mean) and standard deviation (stdv) between TANSO-FTS-2 and 3 other infrared sounders in the 2O-SONO configuration

Sounder	NO. of 2O-SONO	Period	CO_2 spectral range [K]		Atmospheric window channel [K]		O_3 spectral range [K]		CH_4 spectral range [K]	
			mean	stdv	mean	stdv	mean	stdv	mean	stdv
AIRS	4062	Feb. 2019-June. 2021	0.20	0.25	0.03	1.34	-0.22	1.27	-0.52	1.01
IASI	6886	Feb. 2019-Jul. 2021	-0.05	0.26	-0.10	1.71	-0.08	0.81	-0.04	0.90
TANSO-FTS	116689	Feb. 2019-Oct. 2021	0.12	0.41	-0.17	1.13	-0.13	0.78	-0.51	1.05

Figures:

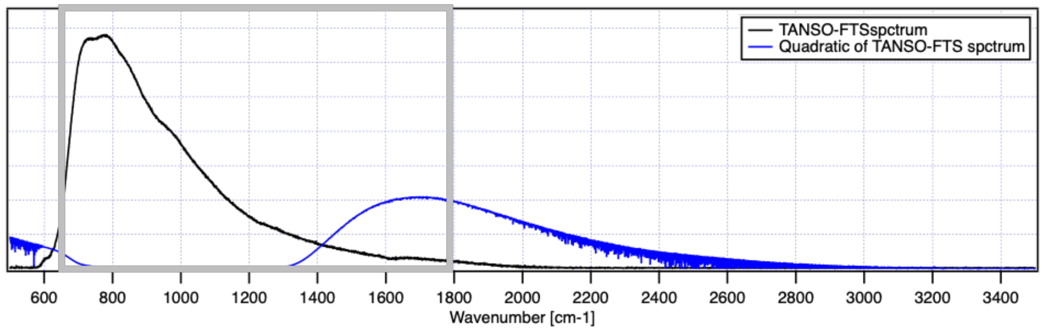

(a) TANSO-FTS

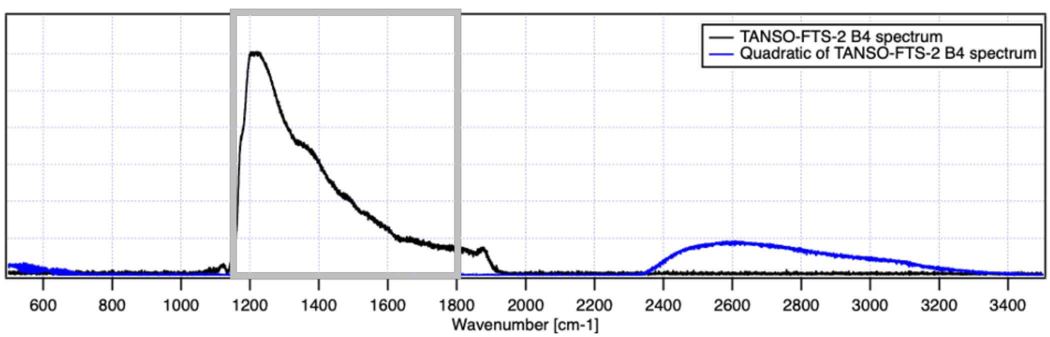

(b) Band 4 of TANSO-FTS-2

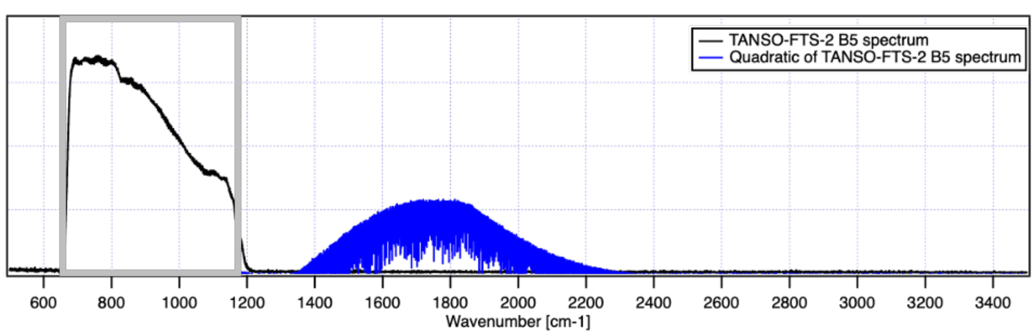

(c) Band5 of TANSO-FTS-2

Figure 1: Non-linear signals on the spectral domain for TANSO-FTS and TANSO-FTS-2. Black lines present the original spectra. Blue lines show $S_b \otimes S_b$ components as the non-linear quadratic term after removing the original spectra. The grey line shows the in-band spectral range for each band.

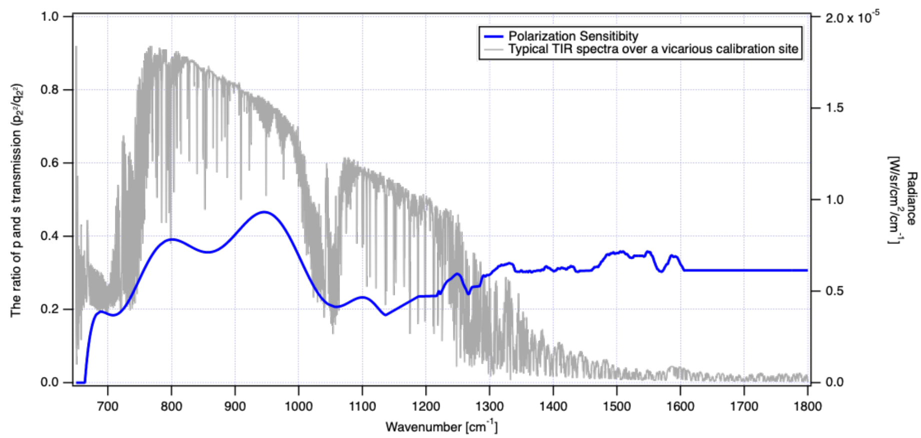

Figure 2: Polarization sensitivity model for bands 4 and 5. The blue line shows the polarization sensitivity as the ratio of p- and s-polarization transmission (p_2^2/q_2^2) against wavenumber. The grey line shows the observed spectral radiance in the TIR band for TANSO-FTS-2.

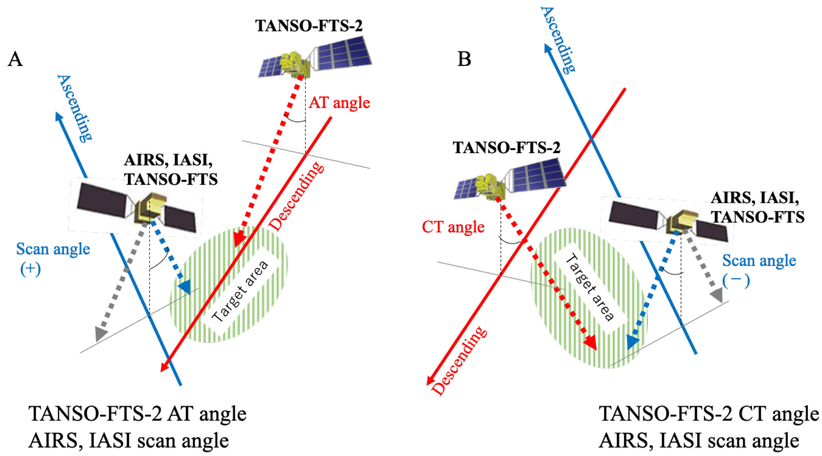

(a) (b)

Figure 3: The schematic diagram for coincident observation between TANSO-FTS-2 and other satellites. (a) the comparison between along-track observation by TANSO-FTS-2 and cross-track observation by other satellites (new method), (b) the comparison between cross-track observation by TANSO-FTS-2 and cross-track observation by other satellite (conventional method).

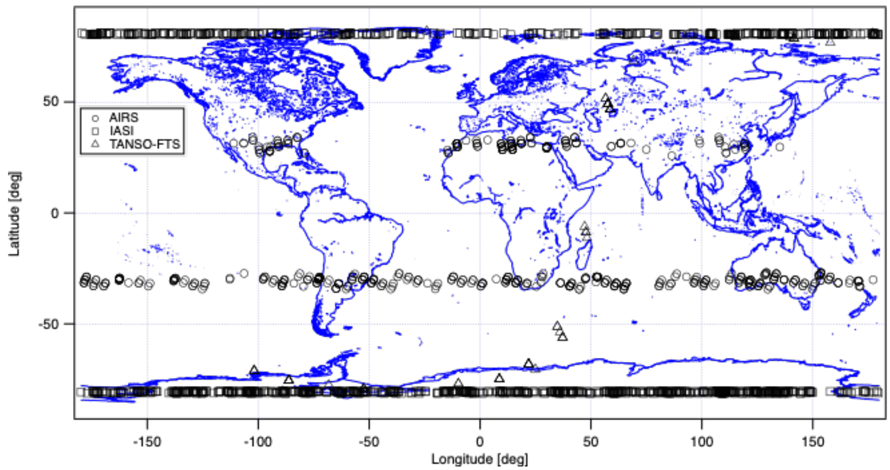

(a)

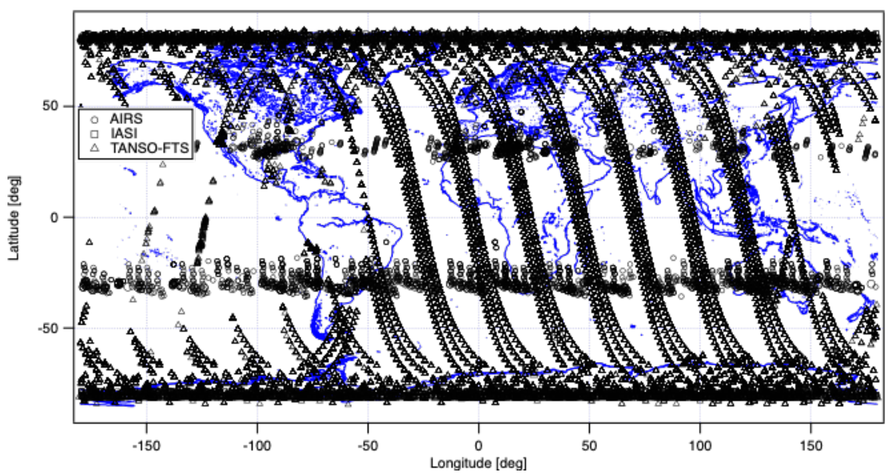

(b)

Figure 4: Comparing TANSO-FTS-2 with other sounders: coincident latitude and longitude map between TANSO-FTS-2 and AIRS/IASI/TANSO-FTS for SNO (a) and 2O-SONO (b).

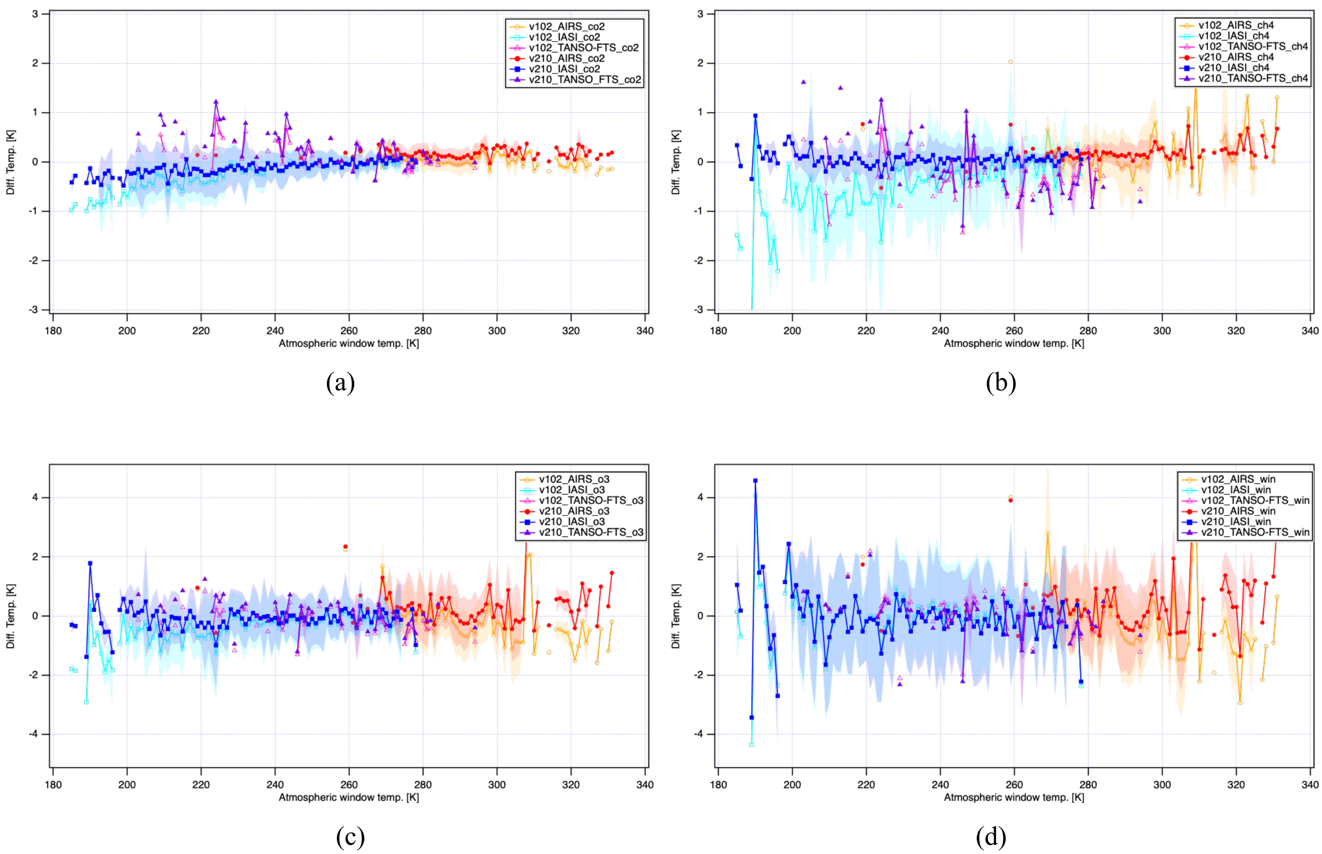

Figure 5: The channel-dependent brightness temperature difference in 1 K bins against atmospheric window temperature for SNO condition between TANSO-FTS-2 and AIRS/IASI/TANSO-FTS. (a) CO_2 spectral range, (b) CH_4 spectral range, (c) O_3 spectral range, (d) atmospheric window channel. The filled dots are the data points, and each shade presents a standard deviation (1σ) for each 1 K bin.

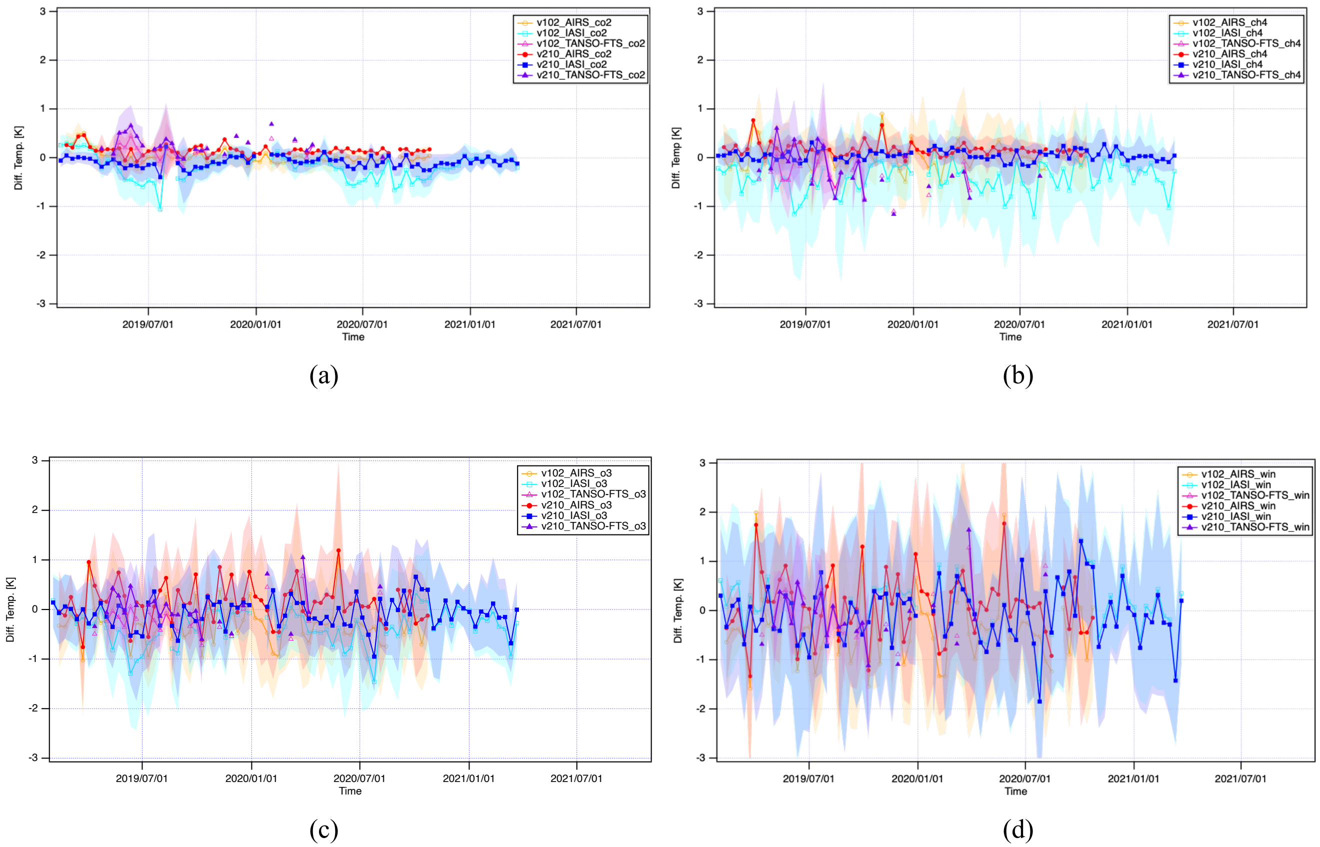

Figure 6: The channel-dependent brightness temperature difference for a ten-day average against atmospheric window temperature for SNO condition between TANSO-FTS-2 and AIRS/IASI/TANSO-FTS. (a) CO_2 spectral range, (b) CH_4 spectral range, (c) O_3 spectral range, (d) atmospheric window channels.

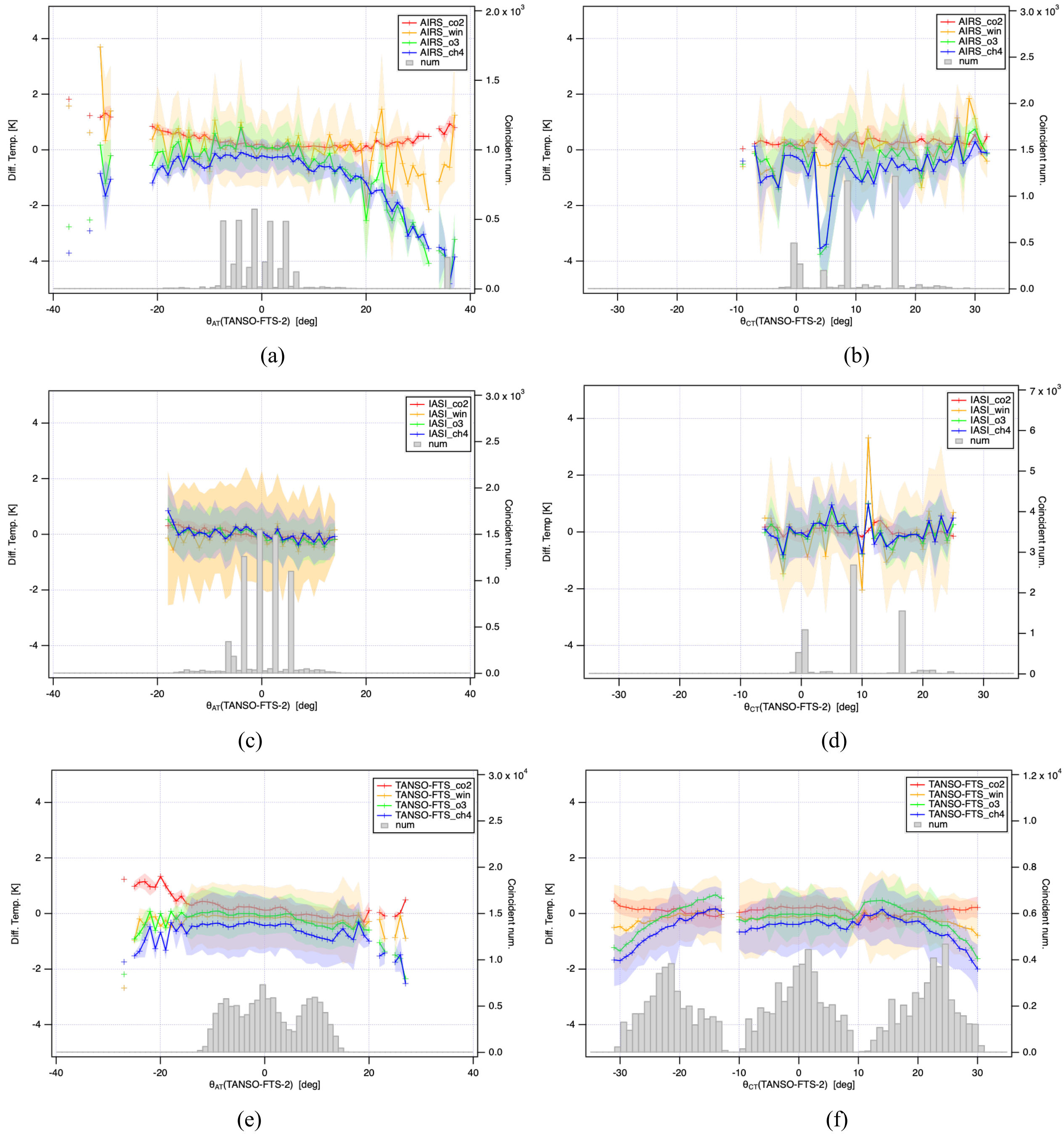

Figure 7: The channel dependent brightness temperature difference in 1° angular bin average against TANSO-FTS-2 θ_{AT} (left) and θ_{CT} (right) for 2O-SONO for AIRS, IASI and TANSO-FTS. The shaded areas present the deviation (1σ) for each grid. The grey bars indicate the number of averaged data in each bin.

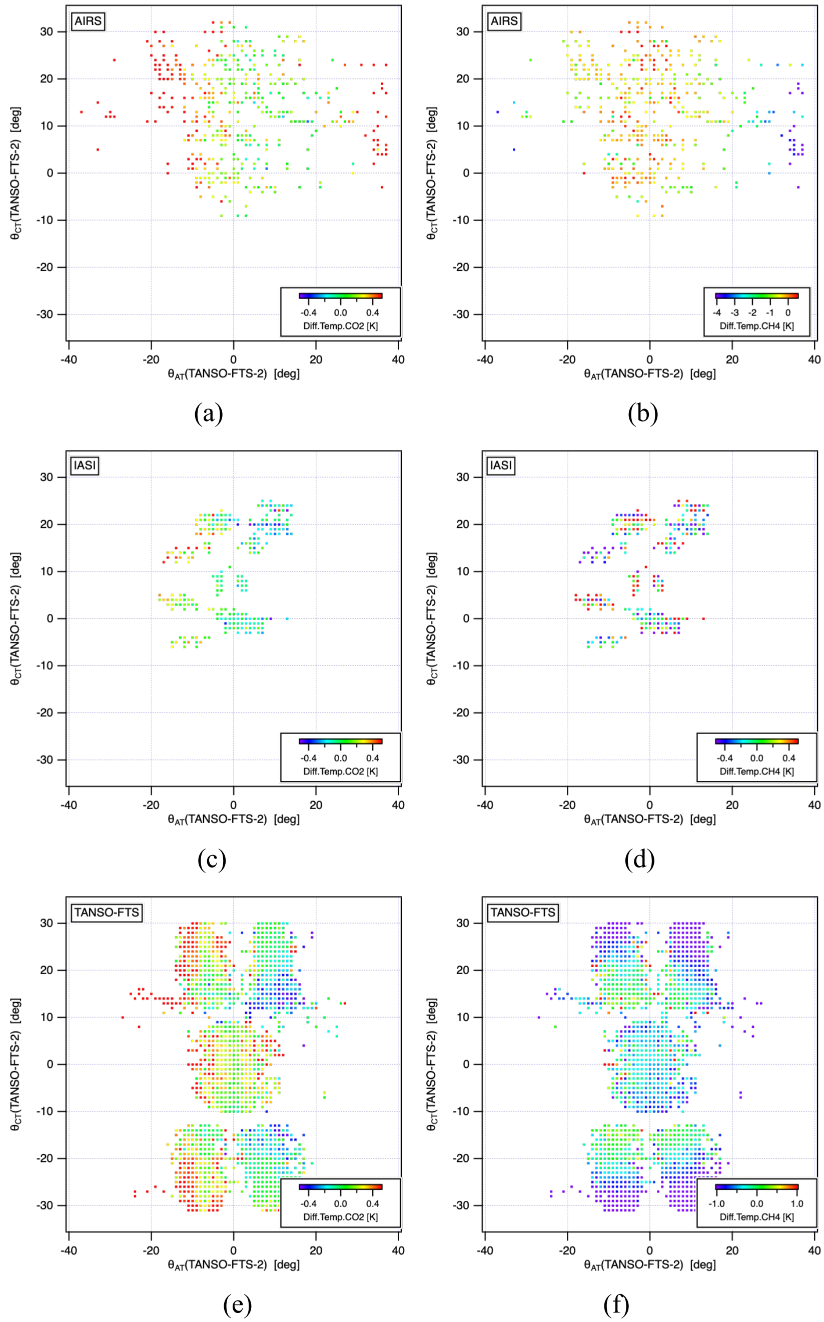

Figure 8: The 1°(θ_{AT}) x1°(θ_{CT}) gridded brightness temperature difference between TANSO-FTS-2 and AIRS/IASI/TANSO-FTS for the CO_2 and CH_4 spectral ranges.

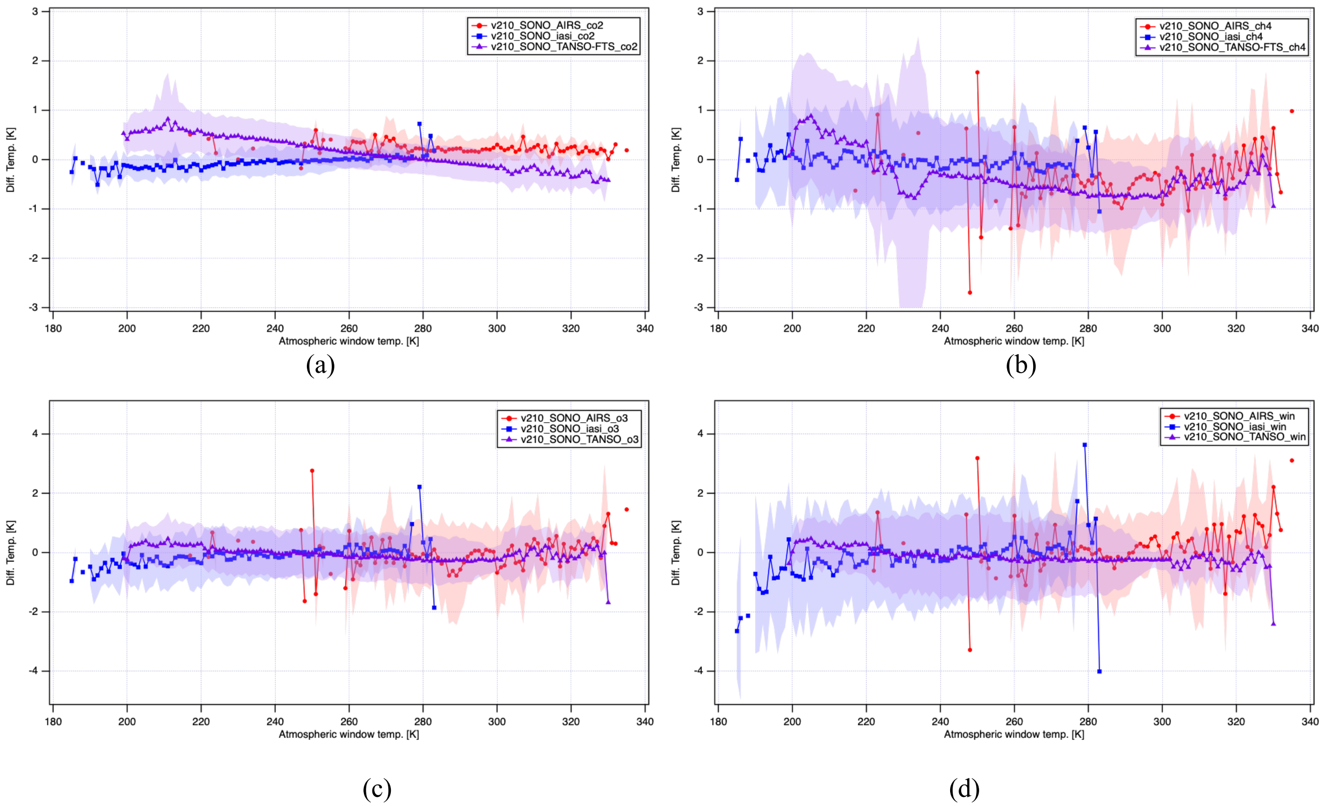

Figure 9: The channel-dependent brightness temperature difference in 1 K bins against window temperature for 2O-SONO between TANSO-FTS-2 and AIRS/IASI/TANSO-FTS with the corresponding standard deviation (shaded area). (a) CO_2 spectral range, (b) CH_4 spectral range, (c) O_3 spectral range, (d) atmospheric window channel.